SPECIAL TOPIC — Smart design of materials and design of smart materials

A thermal conductivity switch via the reversible 2H–1T′ phase transition in monolayer $MoTe_2$

Dingbo Zhang(张定波)[1,2], Weijun Ren(任卫君)[2,3], Ke Wang(王珂)[4], Shuai Chen(陈帅)[2], Lifa Zhang(张力发)[5], Yuxiang Ni(倪宇翔)[1,†], and Gang Zhang(张刚)[2,‡]

[1] *School of Physical Science and Technology, Southwest Jiaotong University, Chengdu* 610031, *China*
[2] *Institute of High Performance Computing, A*STAR* 138632, *Singapore*
[3] *Center for Phononics and Thermal Energy Science, China–EU Joint Laboratory for Nanophononics, School of Physics Science and Engineering, Tongji University, Shanghai* 200092, *China*
[4] *School of Automation, Xi'an University of Posts and Telecommunications, Shaanxi* 710121, *China*
[5] *NNU-SULI Thermal Energy Research Center, and Center for Quantum Transport and Thermal Energy Science (CQTES), School of Physics and Technology, Nanjing Normal University, Nanjing* 210023, *China*

(Received 13 December 2022; revised manuscript received 18 January 2023; accepted manuscript online 10 February 2023)

The two-dimensional (2D) material-based thermal switch is attracting attention due to its novel applications, such as energy conversion and thermal management, in nanoscale devices. In this paper, we observed that the reversible 2H–1T′ phase transition in $MoTe_2$ is associated with about a fourfold/tenfold change in thermal conductivity along the X/Y direction by using first-principles calculations. This phenomenon can be profoundly understood by comparing the Mo–Te bonding strength between the two phases. The 2H-$MoTe_2$ has one stronger bonding type, while 1T′-$MoTe_2$ has three weaker types of bonds, suggesting bonding inhomogeneity in 1T′-$MoTe_2$. Meanwhile, the bonding inhomogeneity can induce more scattering of vibration modes. The weaker bonding indicates a softer structure, resulting in lower phonon group velocity, a shorter phonon relaxation lifetime and larger Grüneisen constants. The impact caused by the 2H to 1T′ phase transition in $MoTe_2$ hinders the propagation of phonons, thereby reducing thermal conductivity. Our study describes the possibility for the provision of the $MoTe_2$-based controllable and reversible thermal switch device.

Keywords: thermal switch, $MoTe_2$, phase transition, thermal conductivity, mechanism

PACS: 05.70.–a, 31.15.A–, 07.10.Cm, 51.20.+d **DOI:** 10.1088/1674-1056/acbaf0

1. Introduction

Two-dimensional (2D) transition-metal dichalcogenides (TMDs) have attracted research attention due to their outstanding mechanical, electrical, magnetic and phonon properties, which makes them promising for use in applications in transistors, sensors and energy conversion devices.[1–3] In recent years, the controllable phase transition of TMDs has intrigued researchers,[4,5] which can undoubtedly promote the development of these high-performance devices.[6,7] The phase-transition-induced changes in the structural, electronic and catalytic properties of TMDs were widely explored.[8,9] The 2H-TMDs can be used in energy storage devices as well as photodetectors, since they are semiconductors with high mobility.[10] In contrast, the 1T-phase exhibits an enhanced hydrogen evolution reaction performance due to its metallic characteristics.[11–13] In practice, the phase transition from the 1T to the 2H phase can be realized through thermal treatment and infrared radiation,[12,13] while the inverse transition is induced by strain and ion intercalation.[14]

Recently, a lithium intercalation method was reported to convert 2H-MoS_2 to 1T-MoS_2, resulting in a small thermal conductivity switching ratio (0.8).[15] The thermal conductivity switching ratio is defined as the ratio between the high (2H-MoS_2) and the low (1T-MoS_2) thermal conductivity values.[16] In addition to gate voltage and strain,[8,17] the 2H–1T–1T′ phase transition of $MoTe_2$ is able to be induced via laser radiation.[18] During this phase transition, the phonon plays a vital role and couples with the laser-activated electrons, showing different phonon behavior in 2H-$MoTe_2$ and 1T′-$MoTe_2$. Compared with the extensive studies on the effect of phase transitions on the electronic and optoelectronic properties of TMDs, the impacts on thermal conductivity are much less explored. Obviously, a better knowledge of the thermal conductivity of different phases can promote our understanding into the physical insights of monolayer TMDs and facilitate its applications over a wide range, including thermal management and thermoelectrics.[19]

Here, based on density functional theory and the Boltzmann transport equation, we studied the thermal conductivities of $MoTe_2$ of the 2H and 1T′ phases, and found that the thermal conductivity of the latter is much lower than that of the former. The underlying mechanism is explained by the

†Corresponding author. E-mail: yuxiang.ni@swjtu.edu.cn
‡Corresponding author. E-mail: zhangg@ihpc.a-star.edu.sg

© 2023 Chinese Physical Society and IOP Publishing Ltd

weaker bonding, bonding inhomogeneity, more scattering of phonons and overall softening of vibrational modes in 1T′-$MoTe_2$. Meanwhile, we demonstrate that 1T′-$MoTe_2$ possesses lower phonon group velocity and stronger anharmonicity than 2H-$MoTe_2$. These results suggest that monolayer $MoTe_2$ can be used as high-performance thermal switches.

2. Simulation methods

The Vienna *ab initio* simulation package (VASP)[20] was used in our calculations. The generalized gradient approximation within the Perdew–Burke–Ernzerhof function is the exchange–correlation function.[21] The convergence criteria for the electronic (ionic) relaxations are 10^{-7} eV (10^{-4} eV/Å).[22] The cutoff energy for the plane wave is 600 eV, the K-mesh is $25\times25\times1$ and the vacuum length is 30 Å.[23]

We obtained the harmonic interatomic force constants (IFCs) using Phononpy[24] and the anharmonic IFCs using thirdorder.py.[25] A $4\times4\times1$ supercell was adopted in the calculations of the harmonic and anharmonic IFCs. Then, the convergence of thermal conductivity was tested from the 4th to 11th-nearest neighboring atoms, as shown in Fig. S1. The results are converged when the cutoff radius reaches 7th-nearest-neighboring atoms. To determine the scale-broad setting and the Q-grid in BTE, their convergences were tested. We found that the results are converged when the scale-broad setting is above 1.00 and the $N_1\times N_1\times1$ is above $60\times60\times1$, as exhibited in Fig. S2. Thus, based on both IFCs, the thermal conductivity was computed using the 7th-nearest neighbors and $60\times60\times1$ Q-grid and 1.0 scale-broad setting, as implemented in ShengBTE.[25] The thickness of the monolayer (H) is the height of the bulk cell in the Z direction divided by the layer number,[26] which are 14.63 Å and 13.59 Å for 2H-$MoTe_2$ and 1T′-$MoTe_2$, respectively, as listed in Table 1.

The relationship of the thermal conductivity (κ_L), specific heat (C), group velocities (v) and relaxation time of the phonon (τ) in ShengBTE is as follows:

$$\kappa_L=\frac{1}{V}\sum\nolimits_i C_i v_i^2\tau_i^{ph},\qquad C_i=\frac{1}{V}\hbar\omega_i\frac{\partial F_0}{\partial T}.$$

Here, V is the volume of the structure, C_i is the specific heat for the phonon mode (i), v_i stands for phonon group velocity of mode i, τ_i^{ph} stands for the relaxation time of mode i, $\hbar$ is the reduced Planck constant, ω_i is the frequency of mode i, F_0 is the Bose–Einstein statistics, and T is the temperature.

$$v_i=\frac{\partial\omega_i}{\partial\boldsymbol{k}_i},\quad\frac{1}{\tau_i^{ph}}=\frac{1}{N}\left(\sum\nolimits^{+}_{i'i''}\Gamma^{+}_{ii'i''}+\sum\nolimits^{-}_{i'i''}\frac{1}{2}\Gamma^{-}_{ii'i''}+\sum\nolimits_{i'}\Gamma_{ii'}\right),$$

where $\boldsymbol{k}$ is the wave vector. Here, $\Gamma^{+}_{ii'i''}$ ($\Gamma^{-}_{ii'i}$) are the three-phonon absorption (emission) scattering rates.

3. Results and discussion

3.1. Structures of 2H-$MoTe_2$ and 1T′-$MoTe_2$

The structures of 2H-$MoTe_2$ and 1T′-$MoTe_2$ exhibit ABA and ABC stackings, respectively. The Mo atom locates in a hexagonal and distorted octahedral coordinate in 2H-$MoTe_2$ and 1T′-$MoTe_2$, respectively, as shown in Figs. 1(a) and 1(b). Interestingly, recent research reported that the two phases could be converted into each other within a short time (∼ ps) via laser radiation.[18] The lattice constants are $a_1=b_1=3.54$ Å for 2H-$MoTe_2$, and $a_2=3.45$ Å, $b_2=6.37$ Å for 1T′-$MoTe_2$, agreeing with previous experimental results,[8,17,27] as listed in Table 1. Then, the bond length was measured in the optimized unit cell. The 2H-$MoTe_2$ has a Mo–Te bonding length of 2.73 Å, while 1T′-$MoTe_2$ shows three Mo–Te bonding lengths of 2.75 Å, 2.79 Å, and 2.84 Å.

Table 1. The calculated lattice parameters (a and b), Mo–Te bonding lengths (L_{Mo-Te}) and monolayer thickness (H) of 2H and 1T′ phases, and the corresponding lattice parameters (a and b) in the previous experimental report.[6]

	a (Å)	b (Å)	L_{Mo-Te} (Å)	H (Å)	a (Å) and b (Å) in the experiment[6]
2H	3.54	3.54	2.73	14.63	$a=b=3.551$
1T′	3.45	6.37	2.75, 2.79, 2.83	13.59	$a=3.452$, $b=6.368$

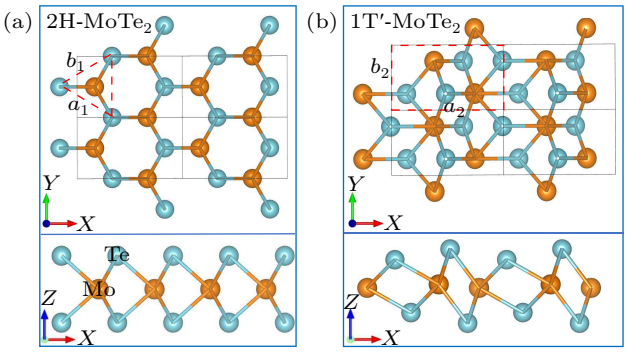


Fig. 1. Top and side views of monolayer (a) 2H-$MoTe_2$ and (b) 1T′-$MoTe_2$. The unit cells are marked by the red dotted line.

To distinguish the differences in Mo–Te bonding between the two phases, we analyzed the overlap between Mo and Te atomic orbitals. It is known that the larger the atomic orbital overlap, the stronger the bonding.[28] The overlap can be quantified by the covalency ($C_{covalency}$) between the atomic orbitals based on the electronic density of states (DOS).[29] As shown in Figs. 2(a) and 2(b), the total electronic DOS of $MoTe_2$ is dominated by Mo-4d and Te-5p orbitals, suggesting that these two orbitals form the Mo–Te bonding. The covalency between Mo-4d and Te-5p is calculated using the following expression:[30]

$$C_{covalency}=-|CM^{Mo}-CM^{Te}|,$$

in which CM^{Mo} is the band center of Mo-4d and CM^{Te} is the band center of Te-5p

$$CM^{\mathrm{Mo}} = \frac{\int_{\varepsilon_2}^{\varepsilon_1} \varepsilon g_{4\mathrm{d}}^{\mathrm{Mo}}(\varepsilon)\,\mathrm{d}\varepsilon}{\int_{\varepsilon_2}^{\varepsilon_1} g_{4\mathrm{d}}^{\mathrm{Mo}}(\varepsilon)\,\mathrm{d}\varepsilon}, \quad CM^{\mathrm{Te}} = \frac{\int_{\varepsilon_2}^{\varepsilon_1} \varepsilon g_{5\mathrm{p}}^{\mathrm{Te}}(\varepsilon)\,\mathrm{d}\varepsilon}{\int_{\varepsilon_2}^{\varepsilon_1} g_{5\mathrm{p}}^{\mathrm{Te}}(\varepsilon)\,\mathrm{d}\varepsilon},$$

where $g_{4\mathrm{d}}^{\mathrm{Mo}}(\varepsilon)$ and $g_{5\mathrm{p}}^{\mathrm{Te}}(\varepsilon)$ are the orbital projected DOS from Mo-4d and Te-5p atomic orbits, respectively.

The covalencies of the 2H and 1T′ phases are −2.15 and −3.36, respectively, indicating that the Mo–Te bonding in 2H-$MoTe_2$ is stiffer than that in 1T′-$MoTe_2$. This result is further verified by the electron localization function (ELF) as shown in Fig. 2(c). The 2H-$MoTe_2$ has stronger bonding, while 1T′-$MoTe_2$ shows three weaker types of bonds (bonding inhomogeneity). Consequently, the weaker bonding and bonding inhomogeneity in 1T′-$MoTe_2$ results in lower thermal conductivity, as shown in the following section.

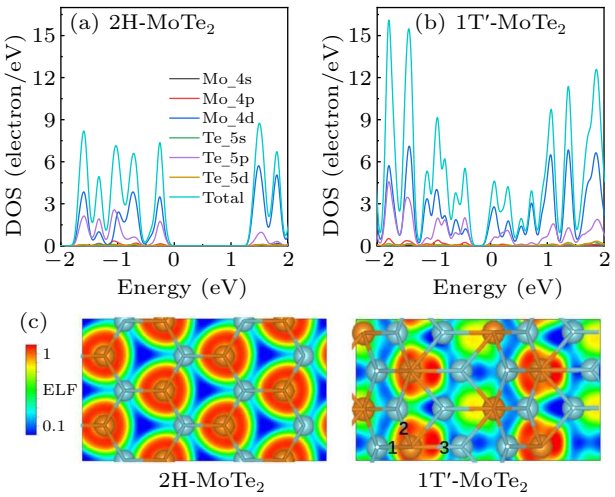


Fig. 2. The total and projected electronic density of states (DOS) of (a) 2H and (b) 1T′ phases, and (c) their electron localization functions (ELFs). The color indicates the relative amplitude of the ELF. The bonding types of 1T′-$MoTe_2$ are identified using Arabic numerals.

3.2. Thermal conductivity of 2H-$MoTe_2$ and 1T′-$MoTe_2$

The thermal conductivity is calculated based on rectangular cells, which are plotted in the gray wireframe in Fig. 1. The 1T′-$MoTe_2$ displays more significant anisotropy in thermal conductivity than 2H-$MoTe_2$ (see Fig. 3(a)). Impressively, 2H-$MoTe_2$ has a larger thermal conductivity along the Y direction than that along the X direction, whereas 1T′-$MoTe_2$ exhibits higher thermal conductivity along the X direction than that along the Y direction. As shown in Fig. 3(b), the thermal conductivities of the 2H (1T′) phase along the X and Y directions are 43.26 (11.98) W/(mK) and 45.84 (4.95) W/(mK) at 300 K, respectively. For the 2H phase, these calculated values are consistent with previous reports.[31] The thermal conductivity switching ratios along the X and Y directions are 3.61 and 9.26 in $MoTe_2$, respectively. Such switching ratios are comparable to, or even higher than, those of the previously reported thermal modulation ratios of MoS_2 (0.8),[15] graphene (2.7),[32] 2D ferromagnets (1.31–5.73),[33] and polymers (8–10),[34] etc.[35,36] Recent research reported that the two phases could be converted into each other within a short time (∼ ps) via laser radiation,[18] gate voltage,[8] and strain.[17] Moreover, the thermal conductivity of 2D materials was measured in many ways, such as via the time-domain heat reflectance method and the laser flash method.[37] Monolayer $MoTe_2$ therefore can be used for high-performance thermal switching devices in practice.

Meanwhile, the contributions of acoustic and optical phonon branches to thermal conductivity are presented in Fig. 3(b). More than 75% of the contribution to thermal conductivity originates from acoustic branches. More convincing evidence can be seen from the cumulative thermal conductivity with frequency, in which phonons at frequencies below 3 THz, i.e., acoustic phonons, mainly contribute to the accumulation of thermal conductivity (see Fig. S3). To further explore the origin of different thermal conductivity between the 2H and 1T′ phases, we next explore the effect of phase transition on the harmonic and anharmonic properties of phonons.

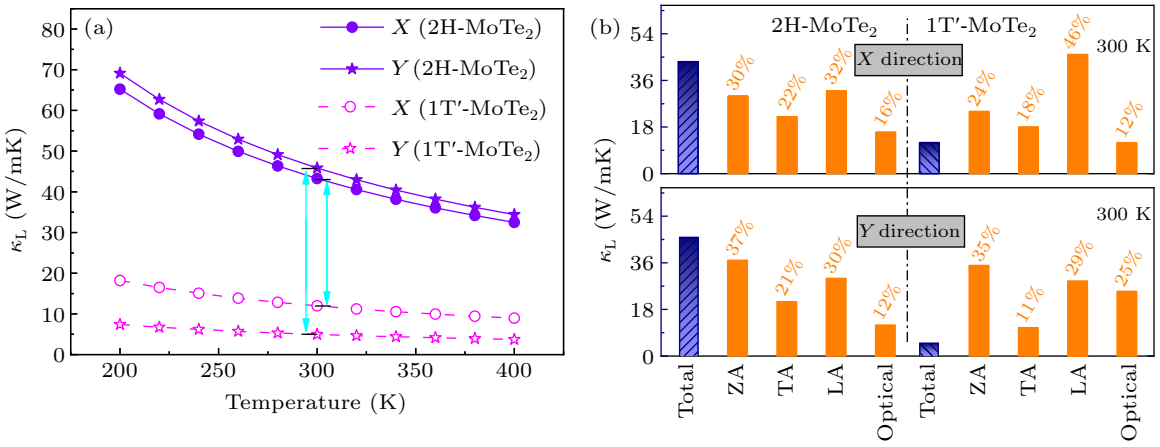


Fig. 3. (a) The thermal conductivities versus the temperature and (b) the thermal conductivities of 2H-$MoTe_2$ and 1T′-$MoTe_2$ at 300 K. The yellow percentages indicate the contributions of out-of-plane (ZA), transverse (TA) and longitudinal (LA) acoustic and optical phonons to the total thermal conductivity.

3.3. Physical insights into the tunable thermal conductivity

Figures 4(a) and 4(b) display phonon dispersions of the 2H and 1T′ phases, respectively. The unit cell of the 2H (1T′) phase has 3 (6) atoms and, accordingly, 9 (18) phonon branches. There are no imaginary frequencies, suggesting dynamical stability. Compared with 2H-$MoTe_2$, 1T′-$MoTe_2$ has a negligible phononic gap between acoustic and optical branches, which enhances the phonon scattering process. Based on the phonon eigenvectors, the phonon vibrational modes of the 2H and 1T′ phases at the *G*-point are illustrated in Figs. S4(a) and S4(b), respectively. The phonon vibrational modes of 1T′-$MoTe_2$ exhibit more directions and weaker strength than those of 2H-$MoTe_2$, showing that the 2H to 1T′ phase transition induces more scattering and overall softening of vibration modes. Consequently, 1T′-$MoTe_2$ has reduced phonon propagation speed and lower thermal conductivity compared with 2H-$MoTe_2$.

Figures 4(e) and 4(f) shows that compared with 1T′-$MoTe_2$, 2H-$MoTe_2$ has higher group velocities of ZA and LA phonons, and lower group velocities of TA phonons. The optical phonon group velocity of 1T′-$MoTe_2$ is larger than that of 2H-$MoTe_2$. Overall, the acoustic phonons of 2H-$MoTe_2$ bear larger group velocities compared with those of 1T′-$MoTe_2$. Therefore, the reduced group velocity with the 2H to 1T′ phase transition is responsible for the lower thermal conductivity in $MoTe_2$.

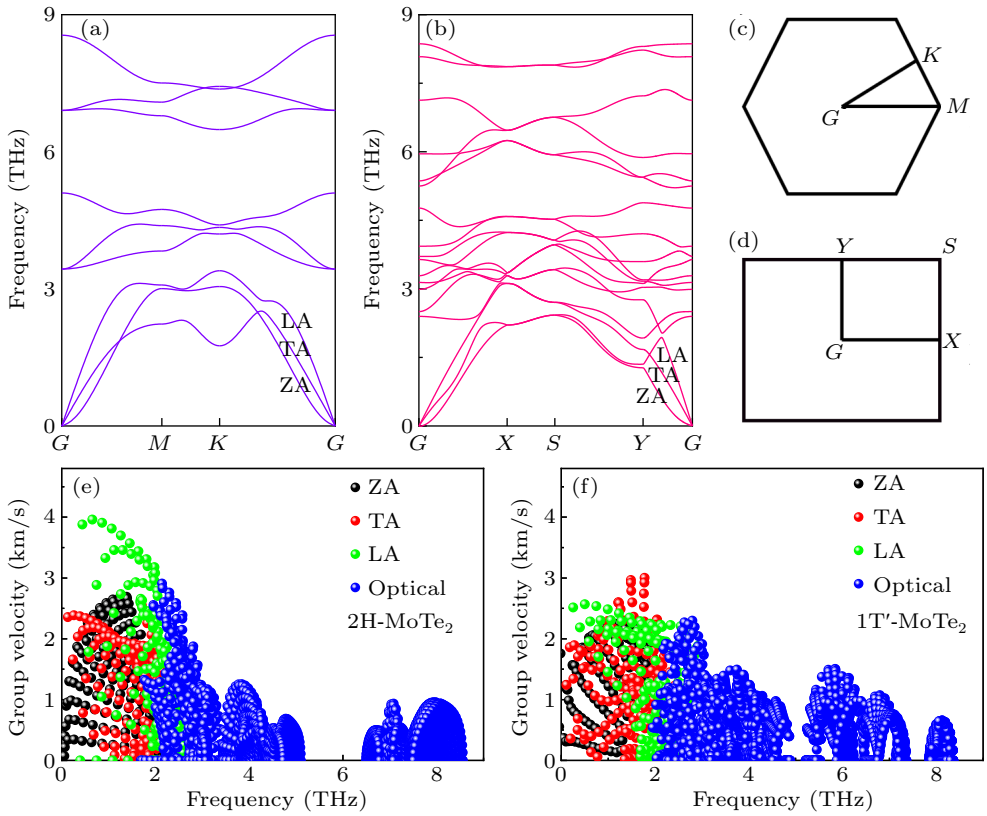


Fig. 4. Phonon dispersions of the (a) 2H-$MoTe_2$ and (b) 1T′-$MoTe_2$ unit cells, and (c), (d) the corresponding Brillouin zone. Phonon group velocity of the (e) 2H and (f) 1T′ phases. LA: in-plane longitudinal acoustic phonons, TA: transverse acoustic phonons, and ZA: out-of-plane flexural phonons.

Phonon relaxation time is an important factor which governs thermal conductivity.[5,38] Figure 5(a) shows that 1T′-$MoTe_2$ shares smaller phonon relaxation time than 2H-$MoTe_2$ over the whole frequency range, which implies that the phonon scattering rate can be reduced by the phase transition from the 2H to the 1T′ phase. This result agrees with our aforementioned analysis of the phonon dispersion. Phonon anharmonicity is important to phonon propagation,[39,40] which is evaluated using the Grüneisen parameter (γ) in this study. The γ is calculated using $\gamma(q) = -\frac{V}{\omega(q)}\frac{\partial\omega(q)}{\partial V}$.[41] As presented in Fig. 5(b), the values of γ for ZA phonons are negative, and those for TA, LA and optical phonons are positive. The main difference in γ between the two phases is the γ of ZA phonons, and the 1T′ phase has a larger γ of ZA than the 2H phase. Therefore, there is a stronger anharmonicity in 1T′-$MoTe_2$, further confirming the lower thermal conductivity.

Finally, we found that the anisotropy in thermal conductivity is attributed to unevenly distributed Mo and Te atoms in the geometric configurations of the rectangular cell. To clearly describe the difference in anisotropic behavior between 2H-$MoTe_2$ and 1T′-$MoTe_2$, we calculated the Grüneisen parameter $\gamma_{q,s}$ for the sth mode using $\gamma_{q,s} = -\frac{a}{2\omega_s(\boldsymbol{q})}\cdot\frac{\mathrm{d}\omega_s(\boldsymbol{q})}{\mathrm{d}a}$ along the

G–Y (X) and G–X (Y) directions (a is the lattice parameter). As shown in Fig. S5, the absolute values of $\gamma_{q,s}$ for the ZA, TA, and LA phonon modes of 1T′-$MoTe_2$ along the Y direction are larger than that of the X direction, as that of 2H-$MoTe_2$ along the X direction is slightly greater than that of the Y direction, which supports our predicted thermal conductivity anisotropy.

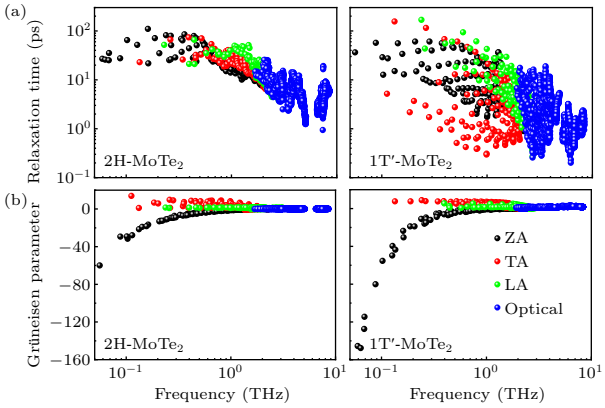


Fig. 5. (a) The phonon relaxation lifetime and (b) the Grüneisen constants of 2H-$MoTe_2$ and 1T′-$MoTe_2$.

3.4. Mechanical properties of 2H-$MoTe_2$ and 1T′-$MoTe_2$

The phonon vibrational modes of a material are closely related to its mechanical properties, and the strength of a mechanical property is measured by Young's modulus.[43] For example, compared with $Y_2Zr_2O_7$, Y_3NbO_7 has a lower Young's modulus, which indicates a softer structure and softening of the vibration modes.[44] Therefore, to provide more insights into the deferent phonon vibrational modes between the two phases, we calculated the Young's modulus based on the elastic modulus tensor.

The stiffness tensor (C_{ij}, $i, j = 1, 2, 6$) is the second partial derivative of the strain energy (E_s) as a function of strain (ε):[45,46]

$$E_s = \frac{1}{2}C_{11}\varepsilon_{xx}^2 + \frac{1}{2}C_{22}\varepsilon_{yy}^2 + C_{12}\varepsilon_{xx}\varepsilon_{yy} + 2C_{66}\varepsilon_{xy}^2,$$

with $\varepsilon = (a - a_0)/a_0$, where a (a_0) is the strained (unstrained) lattice constant. As listed in Table 2, the elastic constants of 2H-$MoTe_2$ are $C_{11} = 83.99$ N/m, $C_{22} = 84.02$ N/m, $C_{12} = 21.43$ N/m, and $C_{66} = 31.15$ N/m, and those of 1T′-$MoTe_2$ are $C_{11} = 61.57$ N/m, $C_{22} = 87.77$ N/m, $C_{12} = 39.66$ N/m, and $C_{66} = 31.42$ N/m, satisfying the Born criteria $C_{11}C_{22} - C_{12}^2 > 0$ and $C_{66} > 0$.[47,48] The structures of both phases therefore display mechanical stability.

Then, the Young's modulus (E) and orientation-dependent Young's modulus (Y) are derived as[49]

$$E_x = \frac{C_{11}C_{22} - C_{12}C_{21}}{C_{22}}, \quad E_y = \frac{C_{11}C_{22} - C_{12}C_{21}}{C_{11}},$$

$$Y(\theta) = \frac{C_{11}C_{22} - C_{12}^2}{C_{11}s^4 + C_{22}c^4 + \left(\frac{(C_{11}C_{22} - C_{12}^2)}{C_{66}} - 2C_{12}\right)s^2c^2},$$

where $s = \sin\theta$ and $c = \cos\theta$. The Young's modulus value of 2H-$MoTe_2$ in the X (Y) direction is 88.52 N/m (88.56 N/m), higher than that of 1T′-$MoTe_2$ (62.22 N/m for the X direction and 43.65 N/m for the Y direction). We find that the stiffness of 1T′-$MoTe_2$ is smaller, confirming the softening of the vibration modes. As shown in Fig. 6, 1T′-$MoTe_2$ exhibits an obvious anisotropic Young's modulus, in which the value in the X direction is much larger than that in the Y direction. On the other hand, 2H-$MoTe_2$ shows little anisotropic Young's modulus, where the value of the Young's modulus in the Y direction is slightly smaller than the value in the X direction. The anisotropy in the Young's modulus complies with the anisotropy of thermal conductivity calculated above.

Table 2. Mechanical properties of 2H-$MoTe_2$, 1T′-$MoTe_2$ and graphene.[42] C_{ij} (in N/m): elastic constants, Y (in N/m): Young's modulus, and v: Poisson's ratio.

	C_{11}	C_{22}	C_{12}	C_{66}	Y_x	Y_y	v_x	v_y
2H-$MoTe_2$	83.99	84.02	21.43	31.15	88.52	88.56	0.26	0.26
1T′-$MoTe_2$	61.57	87.77	39.66	31.42	62.22	43.65	0.45	0.64
Graphene	364.6	364.6	67.3	148.7	352.2	352.2	0.19	0.19

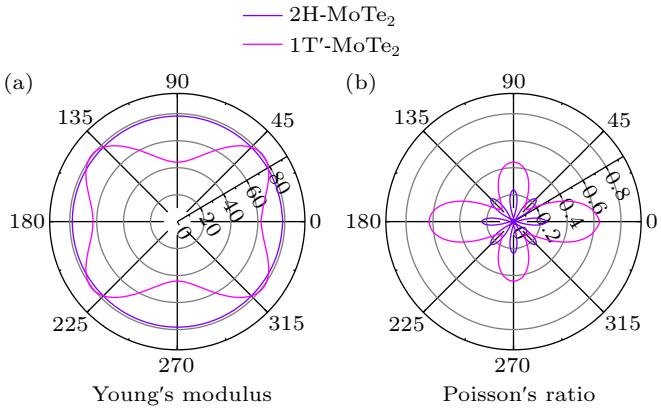


Fig. 6. The orientational-dependent Young's modulus and Poisson's ratio of 2H-$MoTe_2$ and 1T′-$MoTe_2$.

According to the stiffness tensor, the Poisson's ratio (v) and orientation-dependent Poisson's ratio are computed as follows:[49,50]

$$v_{xy} = \frac{C_{21}}{C_{22}}, \quad v_{yx} = \frac{C_{12}}{C_{11}},$$

$$v(\theta) = \frac{C_{12}\left(s^4 + c^4\right) - \left(C_{11} + C_{22} - \frac{(C_{11}C_{22} - C_{12}^2)}{C_{66}}\right)s^2c^2}{C_{11}s^4 + C_{22}c^4 + \left(\frac{(C_{11}C_{22} - C_{12}^2)}{C_{66}} - 2C_{12}\right)s^2c^2}.$$

Both the Poisson's ratios of 2H-$MoTe_2$ along the X and Y directions are 0.26, less than those of 1T′-$MoTe_2$ (0.45/0.64 for the X/Y direction). These values are greater than that of graphene (0.18), implying that 2H-$MoTe_2$ and 1T′-$MoTe_2$ are more flexible than graphene, and ensuring that the two phases can be transformed into each other. It is obvious from Fig. 6 that the values of v vary together with the change of direction, which also demonstrates the anisotropic properties.

4. Conclusion

The thermal conductivities' switching ratio between the 2H and 1T′ phases of $MoTe_2$ reaches 9.26. Such large thermal switching originates from the softening of the structure, smaller group velocity and stronger anharmonicity of the monolayer $MoTe_2$ structure after 2H–1T′ phase transition. Our study qualifies monolayer $MoTe_2$ as an active and reversible thermal switching material with the characteristics of large switching ratios and fast modulation.

Acknowledgments

We gratefully acknowledge the use of the computing resources at the Agency for Science, Technology and Research (A*STAR) and NSCC, Singapore. Project supported by the China Scholarship Council (Grant No. 202107000030), RIE2020 Advanced Manufacturing and Engineering (AME) Programmatic (Grant No. A1898b0043), and A*STAR Aerospace Programme (Grant No. M2115a0092).

References

[1] Yu Y, Nam G H, He Q, Wu X J, Zhang K, Yang Z, Chen J, Ma Q, Zhao M and Liu Z 2018 *Nat. Chem.* **10** 638
[2] Qi K, Cui X, Gu L, Yu S, Fan X, Luo M, Xu S, Li N, Zheng L and Zhang Q 2019 *Nat. Commun.* **10** 1
[3] Yang R, Mei L, Zhang Q, Fan Y, Shin H S, Voiry D and Zeng Z 2022 *Nat. Protocols* **17** 358
[4] Ouyang B, Xiong S, Yang Z, Jing Y and Wang Y 2017 *Nanoscale* **9** 8126
[5] Zhou Y, Xiong S, Zhang X, Volz S and Hu M 2018 *Nat. Commun.* **9** 1
[6] Lai Z, He Q, Tran T H, Repaka D, Zhou D D, Sun Y, Xi S, Li Y, Chaturvedi A and Tan C 2021 *Nat. Mater.* **20** 1113
[7] Torres-Cavanillas R, Morant-Giner M, Escorcia-Ariza G, Dugay J, Canet-Ferrer J, Tatay S, Cardona-Serra S, Giménez-Marqués M, Galbiati M and Forment-Aliaga A 2021 *Nat. Chem.* **13** 1101
[8] Wang Y, Xiao J, Zhu H, Li Y, Alsaid Y, Fong K Y, Zhou Y, Wang S, Shi W and Wang Y 2017 *Nature* **550** 487
[9] Li W, Qian X and Li J 2021 *Nature Reviews Materials* **6** 829
[10] Nasr J R, Simonson N, Oberoi A, Horn M W, Robinson J A and Das S 2020 *ACS Nano* **14** 15440
[11] Deng S, Luo M, Ai C, Zhang Y, Liu B, Huang L, Jiang Z, Zhang Q, Gu L and Lin S 2019 *Angewandte Chemie International Edition* **58** 16289
[12] Gant P, Huang P, de Lara D P, Guo D, Frisenda R and Castellanos-Gomez A 2019 *Materials Today* **27** 8
[13] Deng S, Yang F, Zhang Q, Zhong Y, Zeng Y, Lin S, Wang X, Lu X, Wang C Z and Gu L 2018 *Adv. Mater.* **30** 1802223
[14] Duerloo K A N, Li Y and Reed E J 2014 *Nat. Commun.* **5** 4214
[15] Yang X, Wang S, Wang C, Lu R, Zheng X, Zhang T, Liu M, Zheng J and Chen H 2022 *ACS Applied Materials & Interfaces* **14** 4434
[16] Aryana K, Tomko J A, Gao R, Hoglund E R, Mimura T, Makarem S, Salanova A, Hoque M S B, Pfeifer T W and Olson D H 2022 *Nat. Commun.* **13** 1573
[17] Song S, Keum D H, Cho S, Perello D, Kim Y and Lee Y H 2016 *Nano Lett.* **16** 188
[18] Guan M X, Liu X B, Chen D Q, Li X Y, Qi Y P, Yang Q, You P W and Meng S 2022 *Phys. Rev. Lett.* **128** 015702
[19] Zhang D, Hu S, Sun Y, Liu X, Wang H, Wang H, Chen Y and Ni Y 2020 *ES Energy & Environment* **10** 59
[20] Hafner J 2008 *Journal of Computational Chemistry* **29** 2044
[21] Ernzerhof M and Scuseria G E 1999 *The Journal of Chemical Physics* **110** 5029
[22] Zhang D, Wang K, Chen S, Zhang L, Ni Y and Zhang G 2023 *Nanoscale* **15** 1180
[23] Liu W H, Liu Q J, Zhong M, Gan Y D, Liu F S, Li X H and Tang B 2022 *Acta Materialia* **236** 118137
[24] Togo A and Tanaka I 2015 *Scripta Materialia* **108** 1
[25] Li W, Carrete J, Katcho N A and Mingo N 2014 *Comput. Phys. Commun.* **185** 1747
[26] Qiao J, Kong X, Hu Z X, Yang F and Ji W 2014 *Nat. Commun.* **5** 4475
[27] Hou W, Azizimanesh A, Sewaket A, Peña T, Watson C, Liu M, Askari H and Wu S M 2019 *Nat. Nanotech.* **14** 668
[28] Zhou J, Zhu H, Liu T H, Song Q, He R, Mao J, Liu Z, Ren W, Liao B and Singh D J 2018 *Nat. Commun.* **9** 1
[29] Wang K, Zhou W, Cheng Y, Zhang M, Wang H and Zhang G 2021 *Nanoscale* **13** 10882
[30] Cammarata A and Rondinelli J M 2014 *The Journal of Chemical Physics* **141** 114704
[31] Shafique A and Shin Y H 2017 *Physical Chemistry Chemical Physics* **19** 32072
[32] He J, Li D, Ying Y, Feng C, He J, Zhong C, Zhou H, Zhou P and Zhang G 2019 *npj Computational Materials* **5** 47
[33] Pandey T, Peeters F and Milošvić M 2022 *2D Materials* **9** 015034
[34] Shrestha R, Luan Y, Shin S, Zhang T, Luo X, Lundh J S, Gong W, Bockstaller M R, Choi S and Luo T 2019 *Science Advances* **5** eaax3777
[35] Shin J, Sung J, Kang M, Xie X, Lee B, Lee K M, White T J, Leal C, Sottos N R and Braun P V 2019 *Proc. Natl. Acad. Sci. USA* **116** 5973
[36] Ishibe T, Kaneko T, Uematsu Y, Sato-Akaba H, Komura M, Iyoda T and Nakamura Y 2022 *Nano Lett.* **22** 6105
[37] Song H, Liu J, Liu B, Wu J, Cheng H M and Kang F 2018 *Joule* **2** 442
[38] Shiomi J, Esfarjani K and Chen G 2011 *Phys. Rev. B* **84** 104302
[39] Chang C and Zhao L D 2018 *Materials Today Physics* **4** 50
[40] Li K, Cheng Y, Dou M, Zeng W, Volz S and Xiong S 2022 *Nanomaterials* **12** 123
[41] Zhang Z, Ouyang Y, Cheng Y, Chen J, Li N and Zhang G 2020 *Physics Reports* **860** 1
[42] Zhong H, Huang K, Yu G and Yuan S 2018 *Phys. Rev. B* **98** 054104
[43] Zhang D, Hu S, Liu X, Chen Y, Xia Y, Wang H, Wang H and Ni Y 2020 *ACS Applied Energy Materials* **4** 357
[44] Yang J, Qian X, Pan W, Yang R, Li Z, Han Y, Zhao M, Huang M and Wan C 2019 *Adv. Mater.* **31** 1808222
[45] Zhong H, Yang M, Tang G and Yuan S 2020 *ACS Energy Letters* **5** 2275
[46] Ni Y, Zhang D, Liu X, Wang H, Chen Y, Xia Y and Wang H 2021 *The Journal of Chemical Physics* **155** 204701
[47] Gürel T, Sevik C and Çağn T 2011 *Phys. Rev. B* **84** 205201
[48] Wu C W, Ren X, Xie G, Zhou W X, Zhang G and Chen K Q 2022 *Phys. Rev. Applied* **18** 014053
[49] Zhang D and Hu Y 2021 *Appl. Surf. Sci.* **554** 149608
[50] Zhang D, Hu Y, Zhong H, Yuan S and Liu C 2019 *Nanoscale* **11** 13800